Dual-porosity poroelastic approach to behaviour of porous media over a mining panel

Mao Bai and Derek Elsworth

Synopsis

A dual-porosity poroelastic model is presented with the emphasis on identifying the effect of interaction between fractures and porous matrix on the change in fluid pressure and solid deformation as a result of mining. In a case study the finite-element method is used to approximate the formulation of fluid flow and stress change in the fractured media and a quasi-steady-state leakage function is used to describe the transfer of fluid between the fractures and porous blocks. In comparison to a single-porosity poroelastic model the analysis reveals that the dual-porosity model generates larger deformation and produces a substantially different fluid pressure profile in the initial period. The poroelastic behaviour of the porous media is apparently affected by fluid exchange between the fracture phase and the porous matrix phase, resulting in a history of delayed pressure dissipation. The finding of the research is important to the study of the behaviour of fractured porous media during the mining process.

Fractured rock may be considered as a multi-porous medium[1] in which fractures and intervening porous blocks comprise the most obvious components of a dual-porosity system (Fig. 1). Fractures provide high-conductivity conduits that are amenable to rapid hydraulic flows, whereas the porosity of the matrix blocks provides the bulk of the storage capacity. Owing to their high porosity the porous blocks act as feeders to the fracture system.

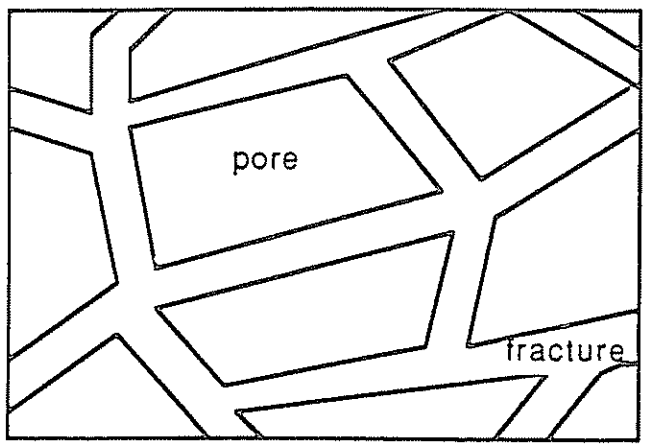

Fig. 1 Morphology of fractured, porous media

The behaviour of naturally fractured media is, therefore, considerably different from that of conventional media that contain only intergranular porosity. In comparison to conventional single-porosity media, dual-porosity media appear to produce more displacement owing to their greater compliance, which is demonstrated by more substantial surface subsidence over a mined area. However, the response of fluid pressure to external disturbance appears to be slower in dual-porosity media owing to the initial interchange of fluid between matrix blocks and fractures. When mining takes place in fractured, porous media the drainage of fluid into a mined void can be sudden and disruptive as a result of this flow between the two types of porosity.

Dual-porosity poroelasticity is a direct extension of the theory of single-porosity poroelasticity that was developed by Biot[2] by application of the theory of mixtures. This extension may be approached in several different ways, but the solutions that are obtained are equivalent.[3–6] Attempts to apply a general expression of the effective stress law in the formulation are reported in the present contribution. The difference between the single-porosity poroelastic model and the dual-porosity model is emphasized. Fluid transfer between fractures and porous matrix is an important aspect of the difference between single- and dual-porosity behaviour. This transfer may be accommodated by an assumed quasi-steady flow that represents an interaction between the fracture and pore phases. In a case study the coupled solid deformation and fluid flow over a mined longwall panel are examined by reference to both steady-state and transient dual-porosity poroelastic models.

Mathematical formulation

The approach to the derivation of a double-porosity model is based on a concept of averaging. The fractured medium is represented by two completely overlapping continua, one representing the porous matrix and the other representing the fracture systems.

The general effective stress law may be described as

$$\sigma'_{ij} = \sigma_{ij} - \phi_m p_m \delta_{ij} \qquad (1)$$

where σ'_{ij} and σ_{ij} are the effective stress and strain tensors, respectively, δ_{ij} is the Kronecker delta, $m = 1$ refers to the fracture phase, $m = 2$ refers to the matrix phase, ϕ_m is the pressure ratio factor for phase m and p is fluid pressure.

The general stress–strain relationship incorporating effective stress effects through pore pressures may be written as

$$\varepsilon_{ij} = \frac{1+\nu}{E}\sigma_{ij} - \frac{\nu}{E}\sigma_{kk}\delta_{ij} - \sum_{m=1}^{2}\frac{\phi_m}{3K_s}p_m\delta_{ij} \qquad (2)$$

where E is the elastic modulus, ν is Poisson's ratio, K_s is the bulk modulus of the rock skeleton, σ_{kk} is total stress, p is fluid pressure and ε_{ij} is the strain tensor. In the present analysis Greek symbols and italicized subscripts take values of 1,2 and 1,2,3, respectively; a comma indicates differentiation and summation is implied over repeated italic subscripts.

Applying the equilibrium relation and the strain displacement relation to equation 1 with the substitution of

Manuscript first received by the Institution of Mining and Metallurgy on 9 December, 1992; revised manuscript received on 22 March, 1993. Paper published in *Trans. Instn Min. Metall. (Sect. A: Min. industry)*, **102**, May–August 1993.

$$G u_{i,jj} + (\lambda + G) u_{k,ki} + \sum_{m=1}^{2} \phi_m p_{m,i} = 0 \tag{3}$$

where G is the shear modulus, λ is a Lamé constant and u is displacement.

In accordance with the continuity requirement that the divergence of the flow velocity be equal to the rate of fluid accumulation per unit volume of space

$$v_{i,i} = \phi_m \dot{\varepsilon}_{kk} - \phi_m^* \dot{p}_m \pm \xi (\Delta p) \tag{4}$$

where ε_{kk} is total strain, ϕ_m^* is relative compressibility and ξ corresponds to a rate of fluid transfer representing the intensity of flow between fractures and pores that is driven by pressure gradient Δp. A positive sign indicates outflow from the matrix and a negative sign indicates inflow into the matrix.

Applying Darcy's law to equation 4 and substituting hydraulic conductivity of phase m yield

$$-\frac{K_m}{\gamma} p_{m,kk} = \phi_m \dot{\varepsilon}_{kk} - \phi_m^* \dot{p}_m \pm \xi (\Delta p) \tag{5}$$

where K_m is the hydraulic conductivity of phase m and γ is the unit weight of the fluid.

Equations 3 and 5 are the governing system equations for the theory of dual-porosity poroelasticity.

Finite-element discretization

A finite-element discretization technique was selected to handle the complicated domain geometries and heterogeneity of materials that are frequently encountered in mining.

Applying the effective stress law of equation 1 enables the stress–strain relationship to be written for a dual-porosity medium as

$$\partial \underline{\sigma} = \underline{D} \left(\partial \underline{\varepsilon} + \sum_{m=1}^{2} \underline{C}\, \underline{m}\, \phi_m \partial p_m \right) \tag{6}$$

where $\underline{\sigma}$ and $\underline{\varepsilon}$ are vectors of stress and strain, respectively, p_m is fluid pressure for phase m, $\underline{C}$ is a compliance matrix, $\underline{D}$ is an elasticity matrix and $\underline{m}$ is a one-dimensional vector. For two-dimensional problems $\underline{m}^T = \{1\ 1\ 0\}$.

Invoking the principle of virtual work and applying the incremental equilibrium to the total stress state result in

$$\int_V \underline{B}^T \partial \underline{\sigma}\, \mathrm{d}v - \partial \underline{f} = 0 \tag{7}$$

where $\underline{B}$ is the strain displacement matrix, $\underline{f}$ is a vector of applied boundary tractions and the integration is completed over the domain V.

Substitution of equation 6 into equation 7 enables the governing finite-element discretization for the solid phase to be given as

$$\underline{K}_T \frac{\mathrm{d}\underline{u}}{\mathrm{d}t} + \underline{R} \frac{\mathrm{d}\underline{p}}{\mathrm{d}t} = \frac{\mathrm{d}\underline{F}}{\mathrm{d}t} \tag{8}$$

where

$$\underline{K}_T = \int_V \underline{B}^T \underline{D}\, \underline{B}\, \mathrm{d}V \tag{9}$$

$$\underline{R} = \sum_{m=1}^{2} \int_V \underline{B}^T \underline{D}\, \underline{C}\, \underline{m}\, \phi_m\, \underline{N}\, \mathrm{d}V \tag{10}$$

and

$$\underline{F} = \int_S \underline{N}\, \underline{f}\, \mathrm{d}S \tag{11}$$

where $\underline{N}$ is a vector of shape functions and S is the domain surface on which surface traction, f, is applied.

Darcy's velocity can be defined as

$$\underline{v} = -K \nabla \left(\frac{\underline{p}}{\gamma} + z \right) \tag{12}$$

where K is hydraulic conductivity, z is the elevation of the control volume and γ is the unit weight of the fluid. The principle of continuity of flow requires that the divergence of the flow velocity vector be equal to the rate of fluid accumulation per unit volume of space. This must include the sum of changes in the total volumetric strain, the change in the solid grain volume and the change in fluid volume due to pressure change. In addition, the volume change due to fluid transfer from the matrix to the fractures or vice versa must be included. The volume changes from all of these sources may be defined as

$$\nabla^T \underline{v} = \underline{m}^T \phi_m \frac{\partial \underline{\varepsilon}}{\partial t} - \phi_m^* \frac{\partial \underline{p}}{\partial t} \pm \xi (\Delta \underline{p}) \tag{13}$$

where $\Delta \underline{p}$ is the fluid pressure difference between the fracture and pore phases.

Substituting equation 12 into equation 13 and invoking the Galerkin finite-element procedure yield the governing equation for the fluid phase as

$$\underline{E}\, \underline{p} + \underline{L} \frac{d\underline{u}}{dt} + \underline{M} \frac{d\underline{p}}{dt} = \underline{Q}^* \Delta \underline{p} + \underline{G}\, \underline{Z} \tag{14}$$

where

$$\underline{E} = -\frac{1}{\mu} \int_V \nabla \underline{N}^T \underline{k}\, \nabla \underline{N}\, \mathrm{d}V \tag{15a}$$

$$\underline{L} = \phi_m \int_V \underline{N}^T \underline{m}^T \underline{C}\, \underline{D}\, \underline{B}\ \mathrm{d}V = \underline{R}^T \tag{15b}$$

$$\underline{M} = -\phi_m^* \int_V \underline{N}^T \underline{N}\, \mathrm{d}V \tag{15c}$$

$$\underline{Q}^* = \xi \int_V \underline{N}^T \underline{N}\, \mathrm{d}V \tag{15d}$$

$$\underline{G} = \int_V \nabla \underline{N}^T \underline{K}\, \nabla \underline{N}\, \mathrm{d}V \tag{15e}$$

Equations 8 and 14 completely define the finite-element formulation of a dual-porosity problem. To form the system of equations it is convenient to express these equations in a matrix form as

$$\begin{pmatrix} \underline{0} & \underline{0} \\ \underline{0} & \underline{E} \end{pmatrix}\begin{pmatrix} \underline{u} \\ \underline{p} \end{pmatrix}+\begin{pmatrix} \underline{K}_T & \underline{R} \\ \underline{R}^T & \underline{E} \end{pmatrix}\begin{pmatrix} \dot{\underline{u}} \\ \dot{\underline{p}} \end{pmatrix}=$$

$$\begin{pmatrix} \dot{\underline{F}} \\ \underline{G} \quad \underline{Z} \end{pmatrix}\pm\begin{pmatrix} \underline{0} \\ \underline{Q}^{\star} \end{pmatrix}\begin{pmatrix} \underline{0} \\ \Delta\underline{p} \end{pmatrix} \tag{16}$$

where, for a two-dimensional formulation

$$\underline{u}=(\underline{u}_1\,\underline{u}_2)^T,\ \underline{p}=(\underline{p}_1\,\underline{p}_2)^T \tag{17}$$

By comparison to the single-porosity formulation[7] it is readily verified that when the fracture spacing that is implied in equation 6 is increased to infinity and the parameters ϕ_1, ϕ_1^* and ξ vanish the dual-porosity model collapses to the single-porosity model.

The continuous time in equation 16 may be approximated by an implicit finite-difference time-discretizing scheme; thus, equation 16 may be written as

$$\begin{pmatrix} \underline{K}_T & \underline{R} \\ \underline{R}^T & \Delta t\underline{E}+\underline{M} \end{pmatrix}\begin{pmatrix} \underline{u} \\ \underline{p} \end{pmatrix}^{t+1}=\begin{pmatrix} \underline{K}_T & \underline{R} \\ \underline{R}^T & \underline{E} \end{pmatrix}\begin{pmatrix} \underline{u} \\ \underline{p} \end{pmatrix}^{t}+$$

$$\begin{pmatrix} \underline{F} \\ \Delta t\underline{G}\underline{Z} \end{pmatrix}^{t+1}+\begin{pmatrix} \underline{F} \\ \underline{0} \end{pmatrix}^{t}\pm\begin{pmatrix} \underline{0} \\ \Delta t\underline{Q}^{\star} \end{pmatrix}\begin{pmatrix} \underline{0} \\ \Delta\underline{p} \end{pmatrix}^{t+1} \tag{18}$$

Flow interaction between fractures and matrix blocks

On the basis of dimensional analysis and the assumption of quasi-steady flow Barenblatt and co-workers[8] deduced that the rate of fluid mass transfer from porous matrix blocks to fractures can be approximated by the quasi-steady-state equation

$$\xi=\frac{\xi_0}{\Pi^2}K\Delta p \tag{19}$$

where Π is an inverse of the specific surface of the fracture (i.e. the surface area of the fracture per unit volume of porous medium) and ξ_0 is a dimensionless constant. Warren and Root[9] defined ξ_0/Π^2 as

$$\frac{\xi_0}{\Pi^2}=\frac{4m_1(m_1+2)}{D_1^2} \tag{20}$$

where $m_1 = 1,2,3$ is the number of normal sets of fractures and D_1 is the characteristic dimension. For three mutually orthogonal fractures $m_1 = 3$; let D_1 equal the fracture spacing, s, and then from equation 20

$$\frac{\xi_0}{\Pi^2}=\frac{60}{s^2} \tag{21}$$

Substituting equation 21 into equation 19 gives

$$\xi=\frac{60K}{s^2}\Delta p \tag{22}$$

Numerical modelling of dual-porosity media

In comparison to the single-porosity model[7] the dual-porosity formulation incorporates an additional flow continuity equation to account for the change of fluid pressures together with the rate of the fluid exchange between fractures and porous media. The representation of flow interaction enables prediction of the time-dependent deformation (consolidation) of porous fractured aggregates. Although the transient effect of fluid flow and solid deformation on structural stability is of prime importance during the mining process, the steady-state, deformation-dependent flow in the fractured porous media may reflect a final effect on the overlying strata following underground mining. Therefore, both steady-state and transient analyses will be conducted with reference to an actual mining case study.[10]

The mine is located in West Virginia, U.S.A. The main aquifer is located approximately 34–40 m below the surface. The decreasing permeabilities that are recorded with depth suggest that secondary porosity (fractures) is dominant in determining the magnitude of the hydraulic conductivity (Table 1). The rock properties were determined primarily by laboratory techniques and the results were scaled to reflect *in-situ* conditions. The coal seam (the Pittsburgh seam) at the mine lies at a depth of approximately 216 m (Fig. 2) and has an average extraction thickness of 1.75 m. The mined panel is 183 m wide by 2195 m long. Development of the longwall panel is affected by two adjacent panels that were extracted at an earlier time (Fig. 3).

Table 1 Parameters for steady-state case

Material	K, m s^{-1} × 10^{-7}	E, MPa	Poisson's ratio
1	32.19	7.52	0.28
2	8.02	16.52	0.25
3	2.41	41.56	0.18
4	1.27	22.02	0.22
5	2.36	9.05	0.37
6	1.42	0.01	0.40
7	1.13	94.99	0.10
8	0.76	41.56	0.18
9	2.55	25.71	0.20
10	5.29	25.71	0.20

Steady-state solid deformation and fluid flow

To provide a first approximation the steady-state dual-porosity behaviour of poroelastic media is evaluated ignoring the coupling seepage force and the flow in matrix blocks.

The subsidence that was measured on the survey line 17 months after mining has been selected for comparison (Fig. 4). The substantial subsidence over the seam may be attributed to the effect of adjacent mining. It is noted that the irregular shape of the curve may reflect the presence of a smaller development pillar on the tailgate side. To match the observed curve by the finite-element method (FEM) the strata that directly overlie the gob were assumed to consist of softer materials than elsewhere as a consequence of caving. The subsidence curve predicted by one of the influence function methods[11] is also plotted in Fig. 4 for comparison. The figure indicates reasonable agreement between the

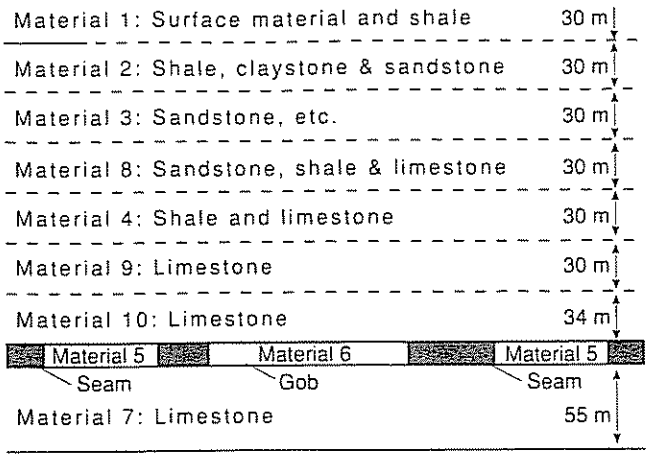

Fig. 2 Lithologies of strata at mine considered in case study

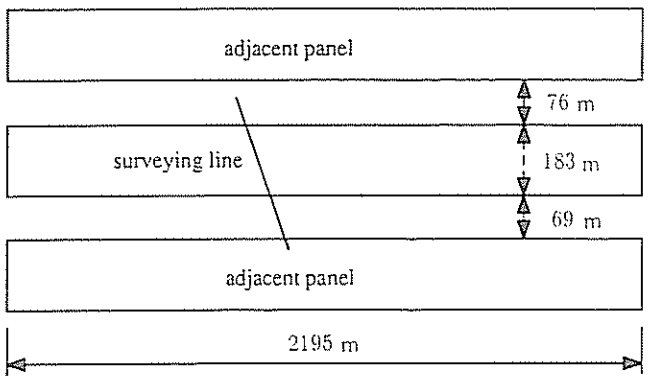

Fig. 3 Layout of mining panels at mine considered in case study

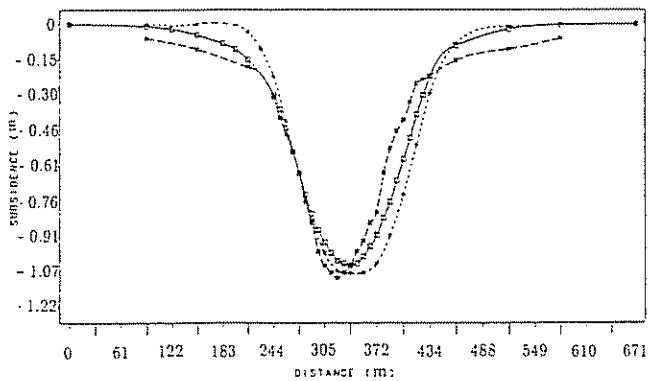

Fig. 4 Surface subsidence: comparison of measured values (*long dashes*) and those predicted by FEM (*solid curve*) and by influence function (*short dashes*)

predictions of subsidence that are obtained with different methods—in particular, over the gob area.

The vertical displacement field over the gob is shown in Fig. 5. The subcritical nature of the subsidence trough can be viewed as the result of a narrowly bounded subsidence domain over the gob, reflecting the effect of caving on the overlying strata. Large, vertical displacements are primarily confined to regions close to the mining level.

Comparison can be made between the measured and calculated contours. Fig. 6 depicts measured subsidence contours reported by Orchard;[12] these conform qualitatively to those evaluated in Fig. 5.

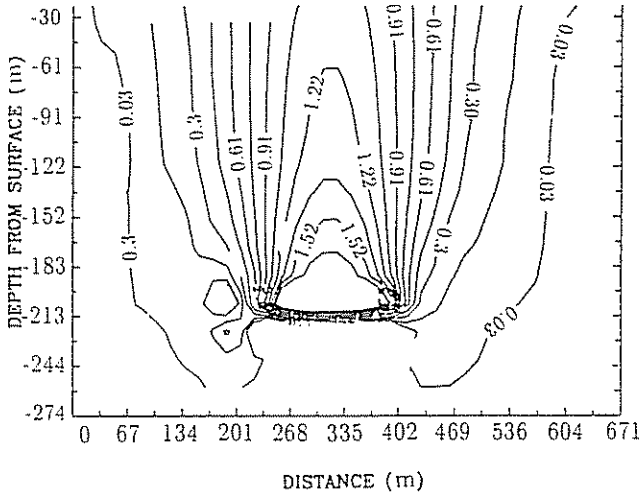

Fig. 5 Predicted subsidence over longwall panel (contours, m)

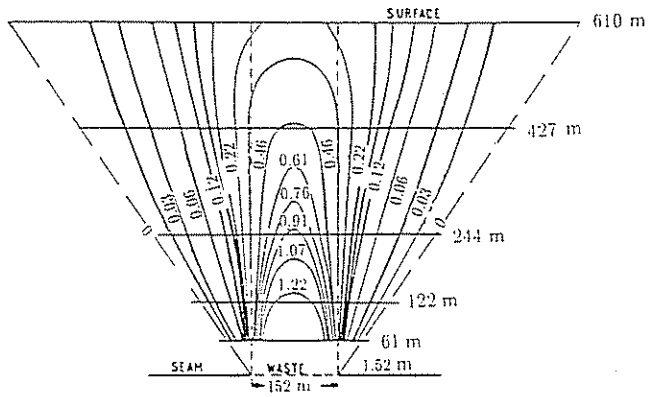

Fig. 6 Measured subsidence over longwall panel (contours, m). (After Orchard[12])

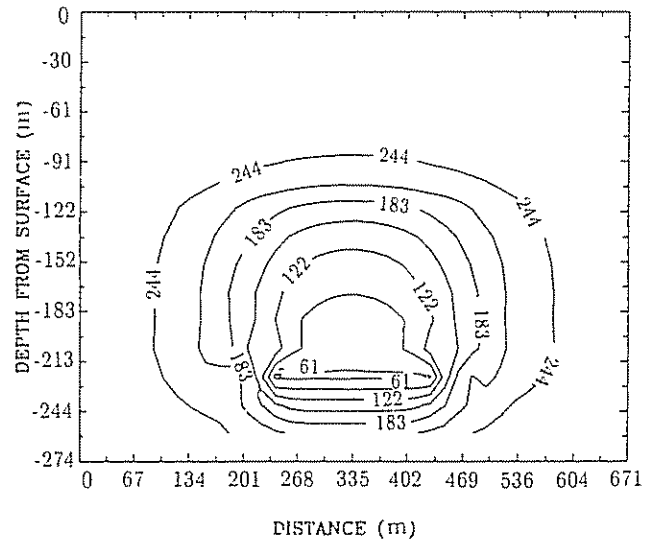

Fig. 7 Predicted hydraulic head over longwall panel, m

Constant head conditions are maintained at the four boundaries of the model as well as at the periphery of the mining panel. The steady head distribution resulting from mining is indicated in Fig. 7, where no modification of hydraulic conductivity is assumed. The equipotential lines demonstrate clearly the direction of fluid flow towards the panel. The calculated distribution of post-mining hydraulic

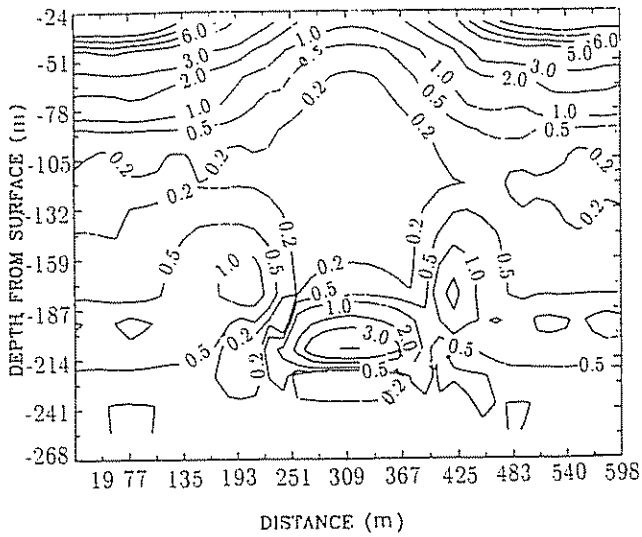

Fig. 8 Predicted vertical hydraulic conductivity (4.72×10^{-7} m s^{-1})

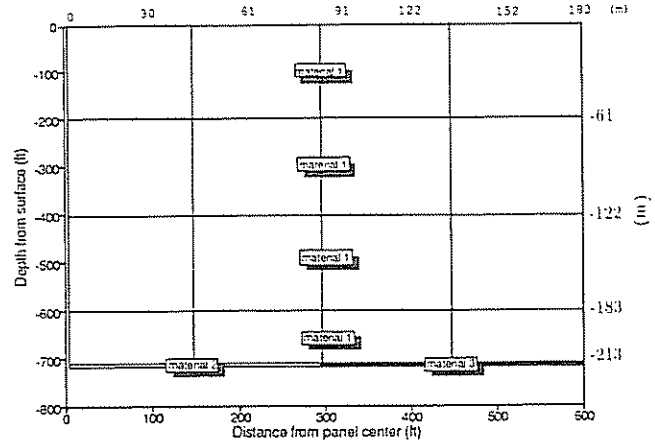

Fig. 9 Mesh layout for finite-element model A

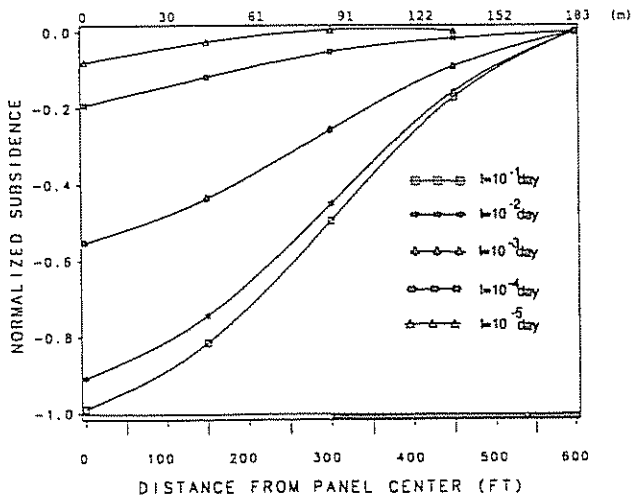

(*a*)

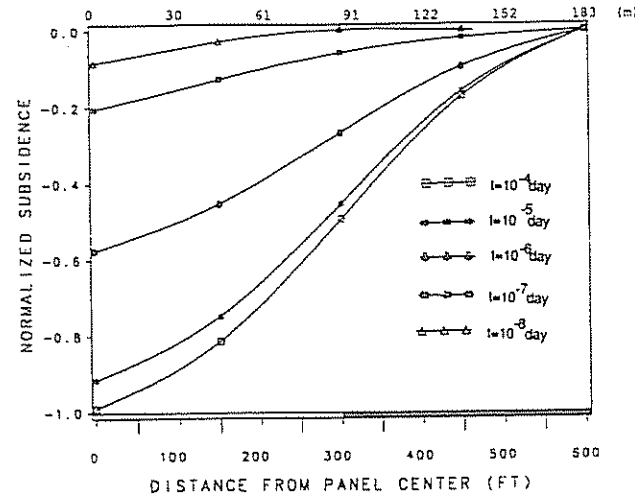

(*b*)

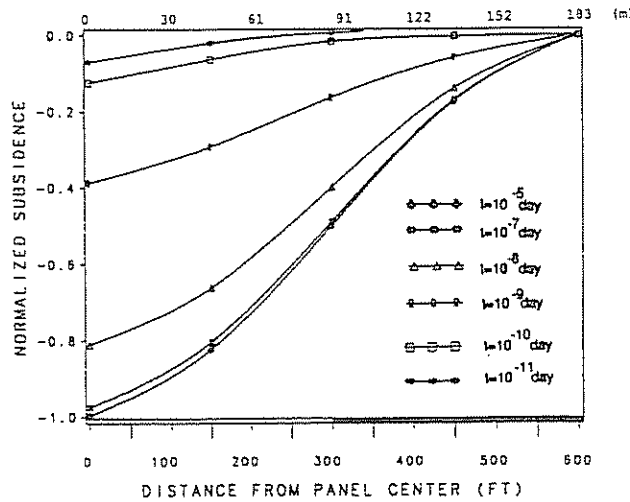

(*c*)

Fig. 10 Surface subsidence with fracture spacing of (*a*) 0.01 m, (*b*) 0.1 m and (*c*) 1 m

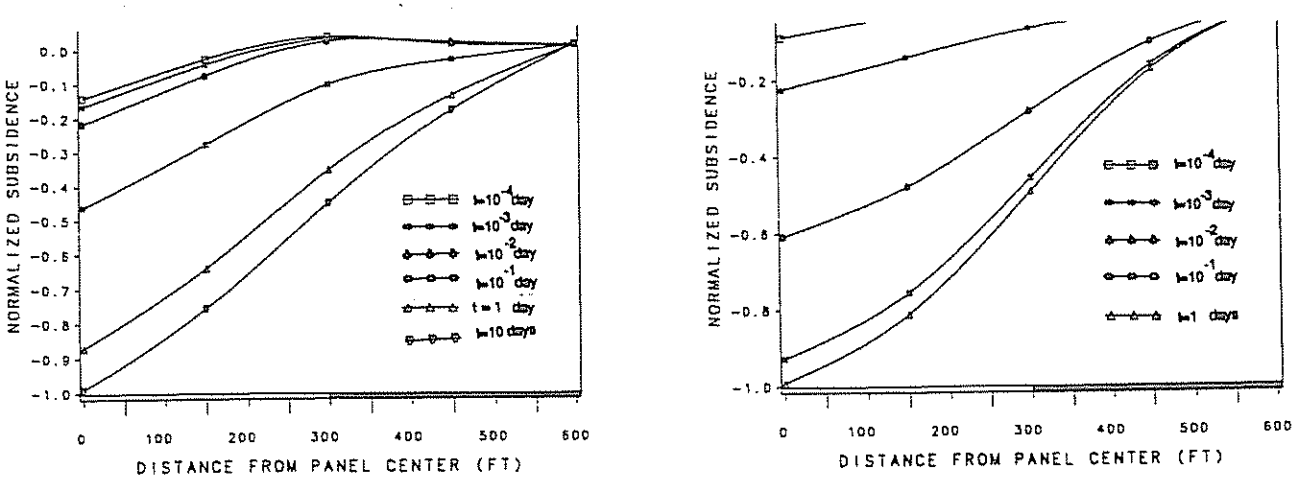

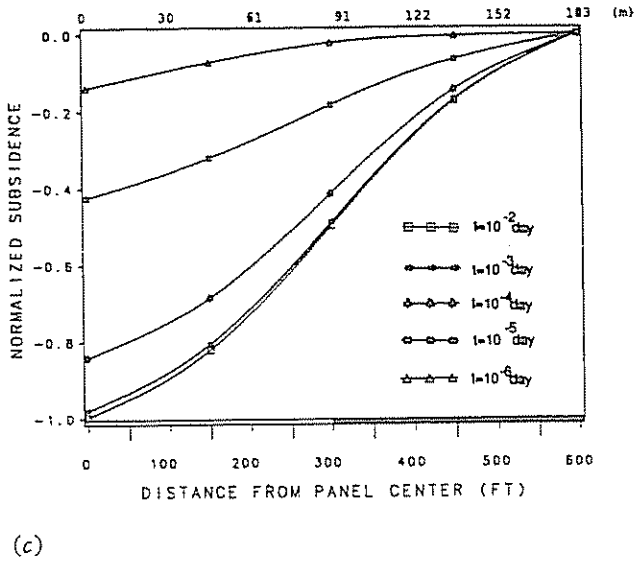

Fig. 11 Surface subsidence with fracture spacing of (*a*) 0.01 m, (*b*) 0.1 m and (*c*) 1 m for softer overburden than considered in Fig. 10

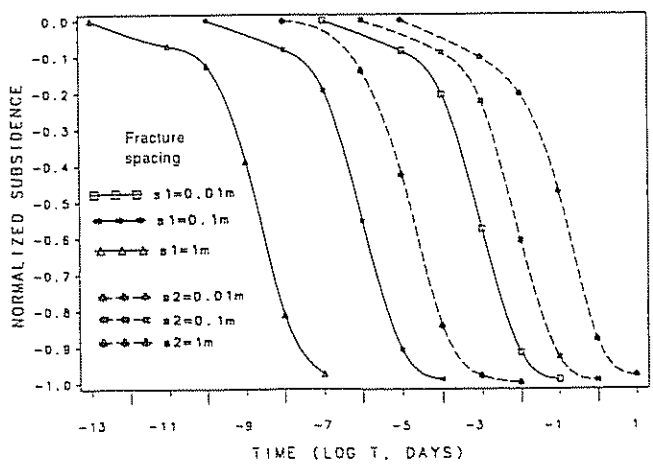

Fig. 12 Maximum surface subsidence 91 m above gob. *Solid curve:* stiffer overburden; *dashed curve:* softer overburden

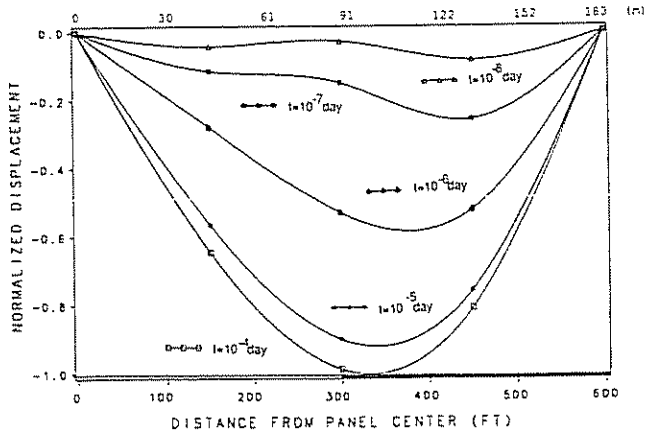

Fig. 13 Surface horizontal displacement with fracture spacing of 0.1 m (stiffer overburden)

conductivity in the vertical direction is shown in Fig. 8 for an assumed fracture spacing, s, of 0.1 m. As expected, the greatest change in hydraulic conductivity occurs in the area immediately over the gob, where large deformations occur as a result. The variation of hydraulic conductivity is strongly dependent on the assumed fracture spacing and ascribed elastic parameters. It is apparent from Fig. 8 that, in contrast to the decrease observed in the ground compression zone, a dramatic increase of vertical conductivity occurs in the surface zone, reflecting the influence of tensile and compressive strains in the surface region.

Transient solid deformation and fluid flow

A finite-element mesh representing a mining panel is shown in Fig. 9. The cross-sectional view is projected where model symmetry is considered. The half-mining width is 91 m. Force boundary conditions are applied at the periphery of the mining panel. Owing to the difference in the assumed number of strata the material properties in the transient case are slightly different from those in the steady-state case. The material parameters that were used in the analysis are listed in Table 2. Parametric studies were completed with fracture spacings of 0.01, 0.1 and 1 m for the stratigraphy shown in Fig 9. Parameters similar to the relative compressibility factor[2] were divided between the different phases; these are $\phi_1^* = 0.05$ and $\phi_2^* = 0.1$. The bulk compressibilities of both grain and fluid were assumed to be zero.

Table 2 Parameters for transient case 1

Material	K_f, m s^{-1} × 10^{-7}	K_r, m s^{-1} × 10^{-7}	E, MPa	Poisson's ratio
1	4.72	0.47	23.94	0.25
2	2.36	0.24	0.24	0.40
3	2.83	0.28	9.58	0.30

Fig. 10 illustrates the increase in surface subsidence with time for three fracture spacings of 0.01, 0.1 and 1.0 m where time, t, is in days. Although the patterns of subsidence given by the various models for the different fracture spacings are similar, the duration of primary consolidation is significantly different.

Further insight into the effect of elastic modulus on the subsidence profile can be gained by using elastic moduli with 1/15 of the values listed in Table 2. The resulting subsidence curves are shown in Fig. 11 for the different fracture spacings. A substantial delay in the consolidation process by comparison with the stiffer model analysed previously is a consequence of using softer material. Results for the surface subsidence at 91 m from the panel centre-line are summarized in Fig. 12, where the maximum subsidence is plotted against various times for both the stiffer medium and the softer medium with various fracture spacings. Fracture spacing has a greater influence on the duration of consolidation as the material becomes progressively stiffer.

Surface horizontal displacement profiles were also investigated. In the example of stiffer overburden with a fracture spacing of 0.1 m (Fig. 13) the maximum surface horizontal displacement curves at various times are not located over the rib of the coal pillar but, rather, are positioned at some distance from the rib. Furthermore, the horizontal displacement curves are irregular at early times of consolidation. This irregularity is probably due to the edge effect of the pillar.

The surface horizontal displacement at 91 m from the panel centre-line at various times is depicted in Fig. 14. As a general observation, it seems that consolidation of between

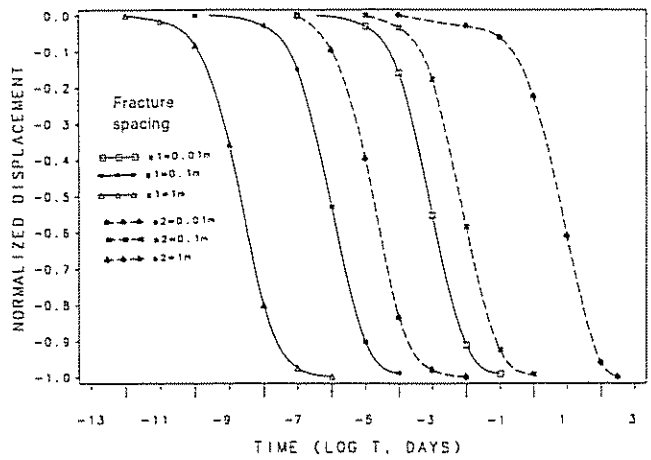

Fig. 14 Maximum horizontal displacement 91 m above mining level. *Solid curve:* stiffer overburden; *dashed curve:* softer overburden

10 and 90% takes about two logarithmic cycles to complete. It can also be concluded that the process in softer media is similar to that in stiffer media but slower. Again, significant delay in the consolidation is demonstrated with both softer and more densely fractured material.

Results obtained with dual- and single-porosity models are compared with field measurements in Fig. 15 at a time equal to 0.1 day. The measured final subsidence curve is confined to the area between the curves for single porosity and dual porosity. Although the single-porosity curve gives a better approximation to the measured curve in terms of the overall subsidence profile, the dual-porosity curve yields a more realistic value for maximum surface subsidence.

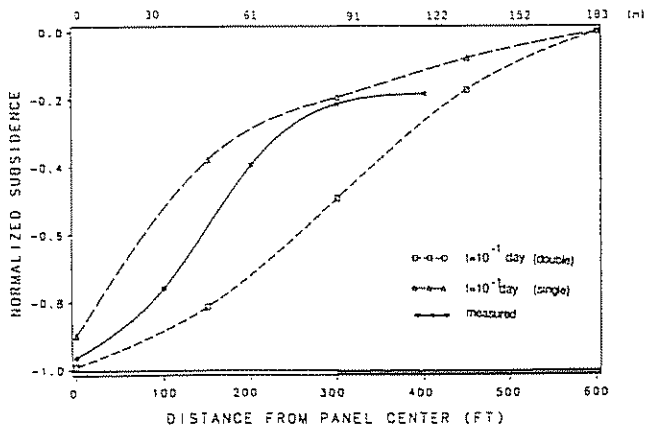

Fig. 15 Surface subsidence: comparison of measured values (*solid curve*) with those predicted by double-porosity model (*short dashes*) and by single-porosity model (*long dashes*)

Surface horizontal displacement with time is plotted in Fig. 16. Again, the dual-porosity model generates larger maximum displacements than the single-porosity model. The maximum horizontal displacement given by the single-porosity model occurs over the gob area, as opposed to the maximum displacement over the pillar that is predicted by the dual-porosity model.

The finite-element mesh for the study of fluid pressure distribution is shown in Fig. 17. The seven material parameters that were used in the analysis are listed in Table 3. Fig. 18 shows the transient change of fluid pressure in fractures when the ratio of fracture permeability to matrix permeability is 10 000. Fluid pressure appears to be most pronounced around the gob. A noticeable change of pressure is also observed over the pillar adjacent to the panel. The

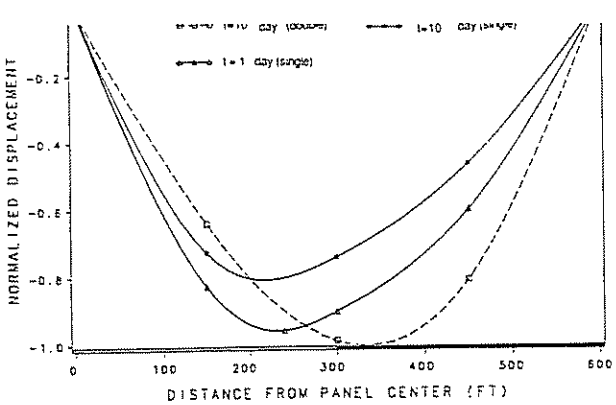

Fig. 16 Comparison of surface horizontal displacements predicted by single- (*solid line*) and double- (*dashed line*) porosity models

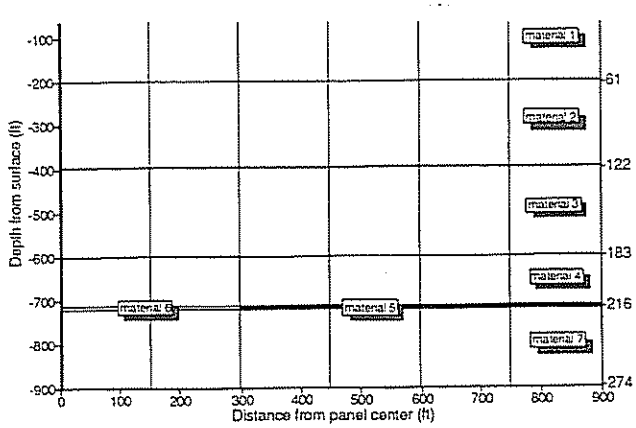

Fig. 17 Mesh layout for finite-element model B

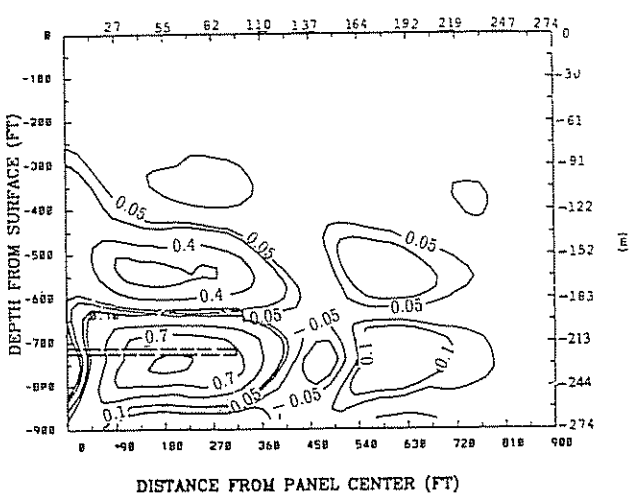

(*a*)

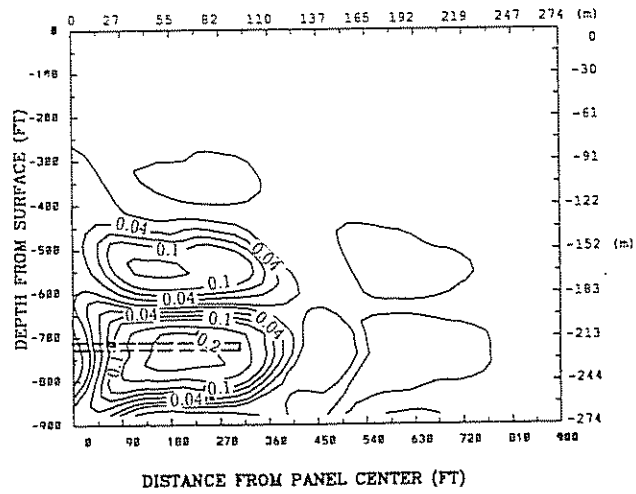

(*b*)

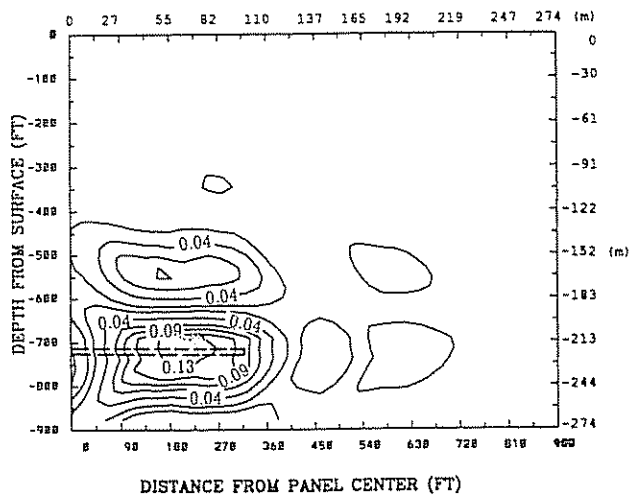

(*c*)

Fig. 18 Dimensionless fluid pressure in fractures for fracture/matrix permeability ratio of 10 000. Time: (*a*) 1 day, (*b*) 10 days and (*c*) 100 days

pressure dissipates more rapidly at a later time, especially in the vicinity of the mining panel.

The pressure interaction between fractures and the porous medium at locations along the centre-line of the panel was investigated on a time-scale of days. The decrease in pressure in fractures in this region after initial loading is plotted in Fig. 19, from which it may be observed that significant fluctuations in pressure occur. A similar pattern, but with substantially reduced magnitudes of fluid pressure, is apparent in the matrix blocks. Fig. 20 indicates the increase in pressure in the porous medium before pressure equalization between fracture and pore phases. A complete history of the pressure within the porous matrix phase is illustrated in Fig. 21. Fluid pressures increase initially (t = 10^{-3}–10^{1} day) until a pressure equilibrium is reached within the fracture phase; subsequently, the pressures dissipate in a

Table 3 Parameters for transient case

Material	K_f, m s^{-1} × 10^{-7}	K_r, m s^{-1} × 10^{-10}	E, MPa	Poisson's ratio
1	20.11	2.01	12.02	0.27
2	1.56	0.16	41.56	0.18
3	1.89	0.19	22.02	0.22
4	5.28	0.53	22.02	0.22
5	2.36	0.24	9.05	0.37
6	1.42	0.14	2.39	0.40
7	3.92	0.39	25.71	0.20

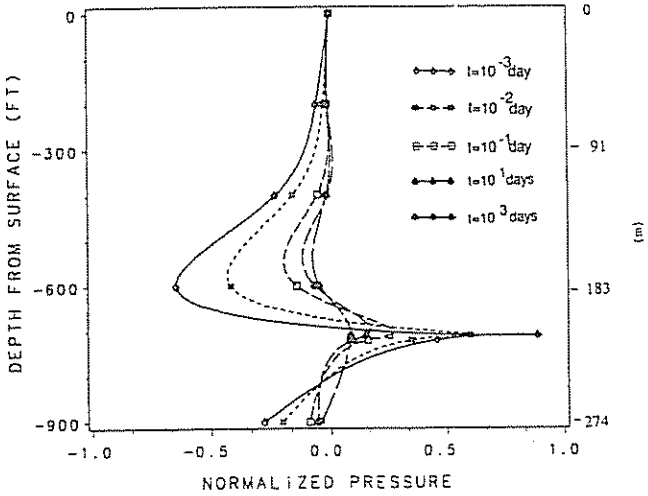

Fig. 19 Normalized pressure dissipation in fractures along panel centre-line after initial loading

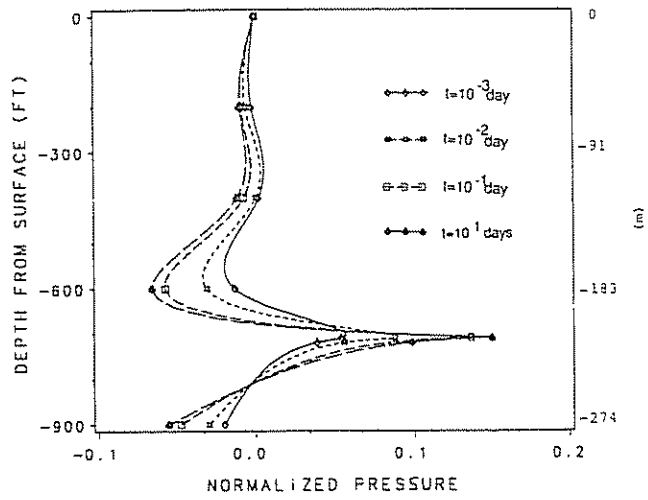

Fig. 20 Normalized pressure increase in matrix

rather different manner until they vanish ($t = 10^3$–10^5 day).

Fracture spacing exerts a controlling influence on the pressure profile. Modification of the fracture spacing in the model depicted in Fig. 17 results in a substantially different distribution of pressure along the centre-line of the panel, as illustrated in Fig. 22. It is interesting to note that a smaller fracture spacing (0.01 m) gives rise to a drastic change in pressure between the surface and the mining panel, whereas a larger spacing (1 m) results in an obvious change in pressure in the gob areas alone.

The permeability ratio is defined as the ratio of the permeability of fractures to that of the porous medium. The variation of this ratio may affect the history of pressure

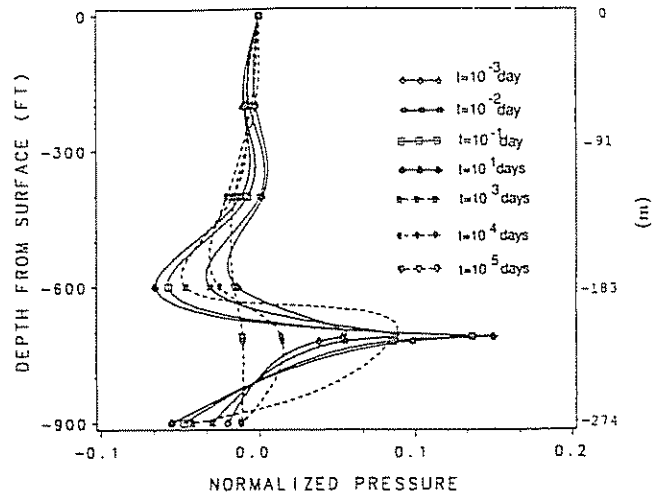

Fig. 21 Complete profile of normalized pressure in matrix

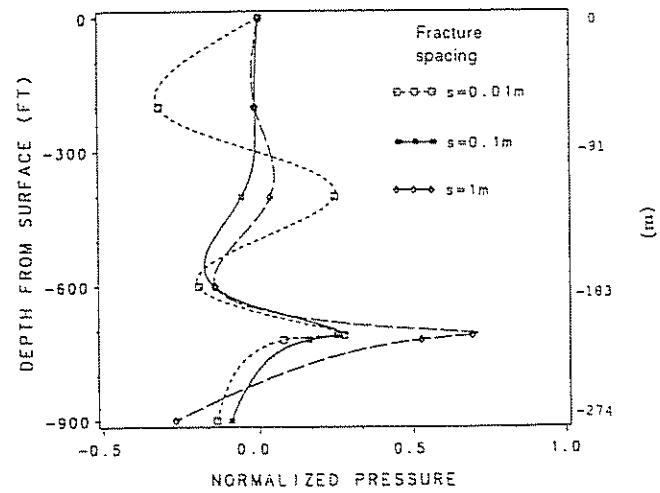

Fig. 22 Pressure in fractures of various spacings along centre-line of panel

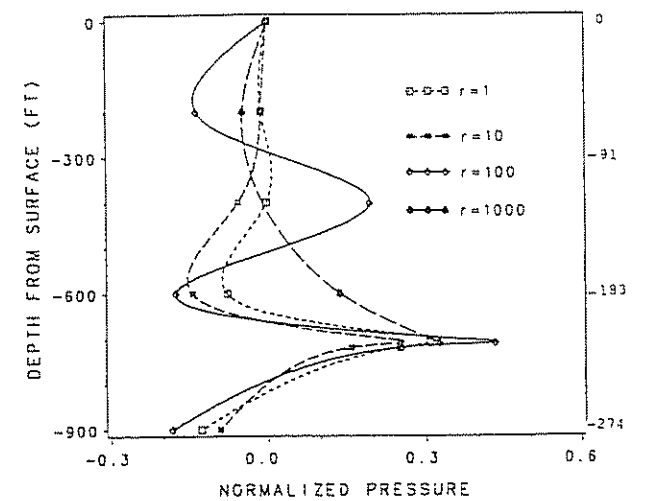

Fig. 23 Pressure in fractures for different values of fracture/matrix permeability ratio, r

interaction between the fracture phase and the porous matrix. Fig. 23 represents the distribution of fracture-fluid pressures along the centre-line of the panel for ratios of 1 to 1000. Despite the dramatic change in the ratio, the induced pressures are highest at the mining level for all values. In the strata between ground surface and gob it appears that the

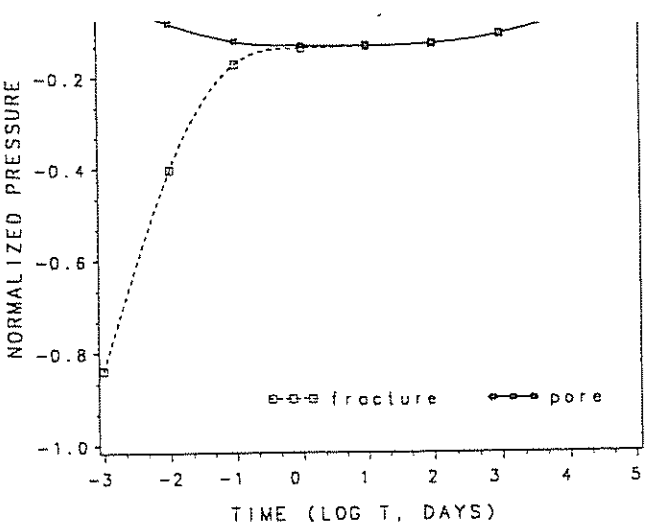

Fig. 24 Normalized pressures in fractures and matrix 30 m above gob on panel centre-line

change in pressure is most pronounced when the ratio is 100, in contrast to the smallest change in pressure for a ratio of unity.

The interactive behaviour of dual-porosity media may alternatively be represented in pressure–time space. Fig. 24 illustrates the history of fluid pressure dissipation at a point on the centre-line 61 m below the surface. The figure indicates that the interchange of fluid between fractures and porous medium is completed approximately one day after initial loading. The pressure remains constant for an extended period of time and subsequently drops until it vanishes. It may be noted that the absolute pressure is always higher in the fracture phase than in the pore phase during the interactive period, owing to the compliance of the fracture phase when subjected to initial loading.

Fluid pressure dissipation behaves in a similar manner for both the single-porosity and the dual-porosity models apart from the absence of the interactive period at an early time for the single-porosity medium. Fig. 25 represents the dissipation of fluid pressure for the two models. The pressure profiles (64 and 34 m, respectively, above the centre-line of the panel) retain a similar trend at large time values. The absolute initial fracture pressure in the dual-porosity model is substantially higher than that in the single-porosity model, indicating the important influence of fracture compressibility. It is also apparent from the figure that the influence of the interaction is greater in regions closer to the mining panel.

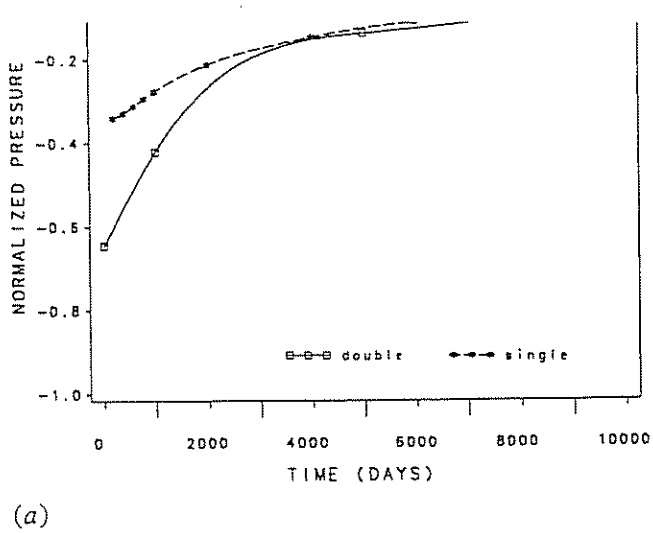

(*a*)

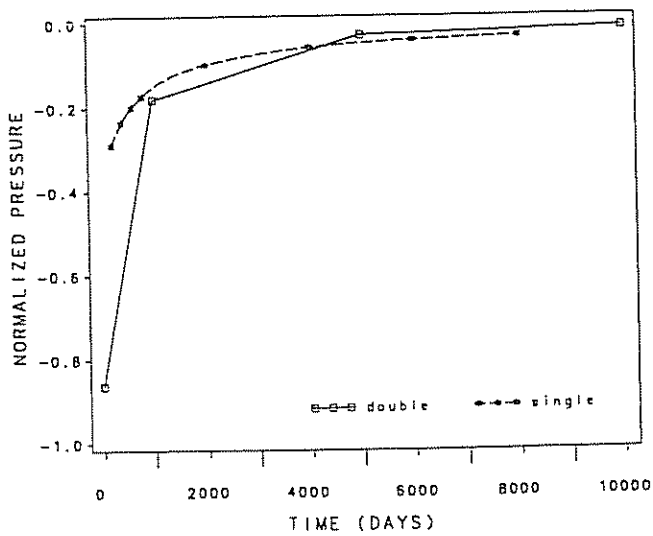

(*b*)

Fig. 25 Comparison of predictions of fluid pressure dissipation by single- and dual-porosity models: (*a*) 64 m above gob; (*b*) 34 m above gob

Concluding remarks

A dual-porosity poroelastic model has been presented as an extension to the single-porosity poroelastic formulation with the object of investigating the behaviour of delayed consolidation as affected by fluid transfer between fractures and a porous matrix. Since behaviour in the dual-porosity model is sensitive to the system parameters, accurate determination of these physical parameters is critical to the successful application of such a model. In practice this requirement is a severe impediment to the application of physically correct dual-porosity models.

(1) The steady-state dual-porosity model shows a strong coupling between strata deformation and fluid flow. The changes in regional hydraulic conductivity occur mainly in the vicinity of the mining panel, where excessive strains due to mining are expected. Less pronounced changes are apparent in the near-surface tension and compression zones.

(2) The dual-porosity models that have been discussed generate larger displacements than the single-porosity model. This may reflect, in large part, the inherent compliance of the dual-porosity medium that results from the compressibility of fractures.

(3) The magnitude of the fluid pressures that are generated is apparently related to the degree of mining influence. Significant changes in fluid pressure are observed in the abutment zone and in the strata adjacent to and overlying the gob. These strata undergo the greatest change in total stress.

(4) Fracture spacing is found to exert a strong influence on the profile of induced fluid pressures. A smaller spacing results in larger induced fracture or matrix pressures in the overlying strata as opposed to a smaller change in the pressure resulting from a larger fracture spacing system.

(5) The study indicates that the change in fluid pressure is largest for a specific permeability ratio (ratio of fracture permeability to matrix permeability).

(6) A comparison of single-porosity and dual-porosity models indicates that the greatest difference in behaviour is seen in the early time period. At later elapsed times, however,

the behaviour of the dual-porosity model conforms closely to the single-porosity medium as fluid transfer between fractures and the porous matrix is reduced.

Acknowledgement

Financial assistance from the Pennsylvania Energy Development Authority and mine data provided by the Consolidation Coal Company Research and Development office are greatly appreciated.

References

1. Aifantis E. C. On the problem of diffusion in solids. *Acta Mechanica,* 37, 1980, 265–96.
2. Biot M. A. General theory of three dimensional consolidation. *J. Appl. Phys.,* 12, 1941, 155–64.
3. Wilson R. K. and Aifantis E. C. On the theory of consolidation with double porosity. *Int. J. Engng Sci.,* 20, 1982, 1009–35.
4. Khaled M. Y. Beskos D. E. and Aifantis E. C. On the theory of consolidation with double porosity—Part 3, a finite element formulation. *Int. J. Numer. Anal. Methods Geomech.,* 8, 1984, 101–23.
5. Elsworth D. Poroelastic response of dual porosity. In *Proceedings Can/Am conference on hydrogeology, Banff, Canada, 1988* (Edmonton, Alberta: Research Council, 1988), 260–6.
6. Elsworth D. and Bai M. Continuum representation of coupled flow-deformation response of dual porosity media. In *Mechanics of jointed and faulted rock* Rossmanith H. P. ed. (Rotterdam: Balkema, 1990), 681–8.
7. Ghaboussi J. and Wilson E. L. Flow of compressible fluid in porous elastic media. *Int. J. Num. Methods Engng,* 5, 1973, 419–42.
8. Barenblatt G. T. Zheltov 1. P. and Kochina N. Basic concepts in the theory of seepage of homogeneous liquids in fissured rocks. *Prikl. Mat. Mekh.,* 24, 1960, 852–64.
9. Warren J. E. and Root P. J. The behavior of naturally fractured reservoirs. *Soc. Pet. Eng. J.,* 3, 1963, 245–55.
10. Hasenfus G. J. Johnson K. L. and Su D. W. H. A hydrogeomechanical study of overburden aquifer response to longwall mining. In *Proceedings 7th Int. Conf. Ground Control in Mining, Morgantown, WV, 1988* (Morgantown: West Virginia University, 1988), 149–62.
11. Liu T. *et al. Coal mine ground movement and strata failure* (Beijing: China Coal Ministry Publishing Company, 1984), 369 p.
12. Orchard R. J. Working under bodies of water. *The Mining Engineer,* 1975, 261–70.

Authors

M. Bai holds degrees of M.Sc. from the University of Newcastle upon Tyne, England, and of Ph.D. from Pennsylvania State University, U.S.A. Currently, he is a research associate in the School of Petroleum and Geological Engineering, University of Oklahoma, U.S.A.

Address: Energy Center, T301, The University of Oklahoma, 100 East Boyd, Norman, OK 73019-0628, U.S.A.

D. Elsworth obtained the degrees of B.Sc. and M.Sc. from Portsmouth Polytechnic and the University of London, England, respectively, and of Ph.D. from the University of California at Berkeley, U.S.A. Currently, he is an associate professor in the Department of Mineral Engineering, Pennsylvania State University, U.S.A.